Delft University of Technology

Unsteady Aerodynamics of Delta Kites for Airborne Wind Energy Under Dynamic Stall Conditions

Castro-Fernández, I.; Cavallaro, R.; Schmehl, R.; Sánchez-Arriaga, G.

Important note
To cite this publication, please use the final published version (if applicable).
Please check the document version above.

RESEARCH ARTICLE OPEN ACCESS

Unsteady Aerodynamics of Delta Kites for Airborne Wind Energy Under Dynamic Stall Conditions

I. Castro-Fernández[1] | R. Cavallaro[1] | R. Schmehl[2] | G. Sánchez-Arriaga[1]

[1]Department of Aerospace Engineering, Universidad Carlos III de Madrid, Leganes-Madrid, Spain | [2]Faculty of Aerospace Engineering, Delft University of Technology, Delft, The Netherlands

Correspondence G. Sánchez-Arriaga (gonzalo.sanchez@uc3m.es)

ABSTRACT

Three unsteady aerodynamic tools at different levels of fidelity and computational cost were used to investigate the unsteady aerodynamic behavior of a delta kite applied to airborne wind energy. The first tool is an in-house unsteady panel method that is fast but delivers low to mid fidelity predictions. The second tool uses the open-source CFD code SU2 to solve the unsteady Reynolds-averaged Navier–Stokes equations with the $k - \omega$ SST turbulence model. At an intermediate level of fidelity, a semiempirical dynamic stall model that combines the panel method with a phenomenological dynamic stall module is proposed. The latter has free parameters that are fine-tuned with CFD results from the second tool. The research on the dynamic stall model has been inspired by two flight test campaigns suggesting dynamic stall phenomena possibly driven by the periodic variation of the angle of attack (aerodynamic pitching motion) during crosswind maneuvers. The recorded inflow along the flight path was prescribed in the three aerodynamic tools. As expected, the price to pay for the low computational cost of the panel method is its inability to capture the dynamic stall phenomenon. The results from unsteady CFD qualitatively matched the experimental data identifying a leading-edge vortex that forms and detaches cyclically during the pitching motion. Using RANS data, the semiempirical tool was fined-tuned to reproduce the dynamic stall behavior, becoming an accurate and fast aerodynamic tool for coupling with any kite flight simulator. Further discussions on the effects of kite aerostructural deflections are included.

1 | Introduction

Airborne wind energy (AWE) systems employ tethered aircraft to convert wind power into electricity or gain traction from the wind. The electricity can be produced on ground (ground-gen systems) by using the pulling force generated by the aircraft or onboard (fly-gen systems) by using onboard turbines. To achieve this, a large variety of technologies have been investigated and developed since the early 2000s [1, 2]. The multidisciplinary nature of AWE systems involve, among others, flight dynamics [3, 4], control [5], and fluid-structure interaction [6, 7] with aerodynamics playing a central role in all of them. In fact, the pioneering work by Loyd [8] already anticipated the great potential of crosswind operation and its sensitivity to the aerodynamic efficiency ($E \equiv C_L/C_D$, with C_L and C_D the lift and drag coefficients of the aircraft). Moreover, the maximum theoretical power for crosswind operation is proportional to C_L^3/C_D^2 [8]. Therefore, a great amount of research effort was put into the numerical aerodynamic modeling and experimental aerodynamic characterization of different AWE aircraft.

Steady aerodynamic tools based on potential flow were broadly applied to AWE systems due to their low computational cost. The lifting-line method was applied to a fixed wing with onboard

---

turbines to investigate the aeroelasticity of a large fly-gen AWE system [9]. The same method was combined with externally derived 2D viscous aerodynamic polars to improve the predictions of the drag coefficient [10,11] and to account for nonlinear corrections of the lift coefficient at stall by using a nonlinear vortex-step method [12–14]. In particular, Candade et al. [13] focused on the three-tether swept kite used by company Enerkíte and realized an aero-structural optimization by coupling the steady nonlinear vortex-step method, a 2+1D finite element model and a bridle model. The major limitation of the lifting-line method is the inherent inability to capture the chordwise lift distribution of the aerodynamic surfaces because the latter are discretized into planar horseshoes (one per chordwise section). For that purpose, the three-dimensional steady vortex lattice method (VLM) was employed to model highly nonplanar wings such as leading-edge inflatable (LEI) kites [15] and morphing wings for AWE applications [6, 16]. Nonlinear stall corrections in the lift and drag coefficients were introduced into a 3D VLM by shedding multiple wakes from prescribed positions of flow separation [17]. Due to its suitability for thick wings, the open-source steady panel method APAME was applied to ram-air kites in an aero-structural framework [18] and box-wing configurations [19]. Besides steady-state analyses, unsteady aerodynamic effects induced by crosswind maneuvers were quantified by applying a 3D unsteady VLM to a rigid-framed delta (RFD) kite [20]. Unsteady effects proved to play a role for highly dynamic AWE maneuvers such as those flown by the delta kite. The unsteady VLM was also useful to generate a reduced-order dynamic model of a fixed-wing AWE system by including the body vortex strengths in the state vector [21]. Potential-flow methods have shown to be a low- to mid-fidelity alternative for aerodynamic modeling of AWE systems but are not accurate tools in scenarios where flow separation is essential.

At a higher fidelity level, the 2D flow field over a LEI kite was solved using steady Reynolds-averaged Navier–Stokes (RANS) simulations with the $k - \omega$ SST turbulence model and the $\gamma - \tilde{R}e_{\theta t}$ laminar to turbulent transition model [22]. The steady-state fluid-structure interaction in LEI kites was also studied by coupling 2D steady RANS simulations for the kite's spanwise sections with a multibody model of the tube kite [23]. A similar steady fluid-structure interaction model was coupled with a dynamic model of the AWE system that also included a flight controller to fly figure-of-eight maneuvers [24]. All the 2D RANS analyses over LEI kites highlighted the importance of using high-fidelity aerodynamic methods to model the recirculation zone behind the leading-edge tube even at low angles of attack and the flow separation on the extrados (suction side). Three-dimensional steady RANS simulations become necessary to capture not only viscous but also three-dimensional effects which are not negligible due to the relatively low aspect ratio and highly nonplanar geometries of AWE kites. Some of the first computational fluid dynamics (CFD) studies on kites solved the 3D steady RANS equations around curved (C-type) wings with a double membrane [25] and a NACA 64-418 sectional shape [15]. The 3D flow around a LEI kite was studied by using steady RANS simulations with the $k - \omega$ SST turbulence model and the $\gamma - \tilde{R}e_{\theta t}$ transition model [26]. An expansion of this work concluded that the effect of chordwise struts in LEI kites is negligible irrespective of the sideslip angle, however, the latter influenced the aerodynamic efficiency of the LEI kite [27].

The steady aeroelastic deformation of a ram-air kite was studied by coupling the 3D RANS equations ($k - \omega$ SST turbulence model) with a membrane-like finite element model [28].

High-fidelity CFD simulations were also applied to fixed-wing AWE systems. A multielement airfoil applied to AWE was aerodynamically optimized using 2D steady RANS [29] and the viscous-inviscid solver MSES together with RANS verifications [30]. The comparison between MSES and RANS in Ko et al. [30] highlighted the need of using a CFD tool to verify a lower-fidelity tool. The 3D aerodynamics of the fixed-wing Ampyx power aircraft was studied through RANS ($k - \omega$ SST turbulence model) [31]. Apart from RANS approximation, the viscous vortex particle method was applied to the Makani M-600 prototype with and without onboard turbines [32]. Regarding fluid-structure interaction, a recent work studied a multimegawatt AWE reference model by coupling a detailed finite element model for the structure with unsteady RANS ($k - \omega$ SST turbulence model and wall-function approximations near the wing) [7]. In Pynaert et al. [7], the full wind window of the AWE system ($620 \times 620 \times 100$ m^3) was solved with unsteady RANS and the vehicle followed a circular crosswind trajectory with a logarithmic wind profile. The latter produced variations in the angle of attack and, consequently, in the lift and drag coefficients highlighting the importance of considering realistic crosswind kinematics as compared with steady conditions in AWE applications. Another remark of Pynaert et al. [7] is the negligible influence of the kite's wake on the aerodynamic coefficients (~ 0.2 %) suggesting that a smaller domain containing the aircraft and its kinematics with respect to the wind may be aerodynamically equivalent.

On the experimental side, several AWE testbeds aiming at the aerodynamic characterization of kites fused data from on-ground and onboard sensors to estimate the state vector of the kite including aerodynamic variables [33–36]. In-flight flow measurements to estimate the aerodynamic velocity, angle of attack and sideslip angle were obtained for the first time with a system composed of vanes and a pitot tube attached to the bridle lines of a LEI kite [34]. Likewise, a more accurate multihole pitot tube was boarded on an RFD kite and the aerodynamic forces and torques were estimated as part of the state vector by using estimation before modeling techniques [36]. Previous works [34, 36] uncovered relevant unsteady aerodynamic and aeroelastic phenomena after observing variations of the angle of attack and aerodynamic coefficients during figure-of-eight maneuvers. Previous studies [36] and [20] proposed the unsteady aerodynamic phenomenon of dynamic stall as a candidate to explain the hysteresis of the experimental aerodynamic coefficients versus the angle of attack in the delta kite. Dynamic stall is an unsteady viscous phenomenon characterized by cyclic separation and reattachment of the flow induced by oscillations in the angle of attack. However, no experimental observation of the periodic flow separation in AWE systems has been made to date. Both CFD codes and semiempirical dynamic stall models have been extensively used to simulate this phenomenon. Semiempirical dynamic stall models combine potential-flow theory with a set of phenomenological dynamic equations with free empirical parameters at a lower computational cost than CFD simulations. The well-known semiempirical dynamic stall models of Tran and Petrot [37] (ONERA model), and Leishman

and Beddoes [38] (Leishman–Beddoes model) were employed to model the aerodynamic responses of helicopter [39] and wind turbine [40] blades. Among the various modifications of the Leishman–Beddoes model, Hansen et al. [41] considered the unsteady effects in the aerodynamic coefficients as variations about the steady values, improving the agreement between the dynamic stall model and the high-fidelity data, and Boutet et al. [42] modified the Leishman–Beddoes model to account for low Reynolds and low Mach numbers.

Since used by some companies and universities like Enerkíte [13] and UC3M [20, 36, 43], delta wings and kites are particularly interesting for AWE applications. In addition, their high maneuverability leads to highly dynamic crosswind maneuvers. For this reason, this work carries out a detailed unsteady aerodynamic analysis of RFD kites by combining experiments and numerical simulation with two objectives: (i) uncover dynamic stall phenomena during the figure-of-eight maneuvers and (ii) develop an accurate aerodynamic model with a low computational cost. With this aim, it is first shown in Section 2 that the experimental lift and drag coefficients of RFD kites versus the angle of attack exhibit hysteresis repeatedly in the figure-of-eight trajectories measured in the experiments. Moreover, an in-situ flow visualization experiment revealed a cyclic flow separation on the kite extrados and strong deformations of the central bar (spine) and canopy of the delta kite. Because to the best of the authors' knowledge dynamic stall was not studied before for AWE applications through numerical simulations, Section 3 presents three aerodynamic models at different levels of fidelity and computational cost. The first model is the 3D unsteady panel method (UnPaM) presented in Castro-Fernández et al. [20] with novel modifications of the wake that improve the prediction quality of the tool. The second model solves the unsteady incompressible RANS equations with the $k-\omega$ SST turbulence model of the open-source code SU2 [44–46]. The third model, which has a degree of fidelity and computational cost between the first and second, is a semiempirical dynamic stall model that combines UnPaM with a phenomenological dynamic stall module. Such a module has free parameters that were fine-tuned by using steady and unsteady RANS results from the second tool. In Section 4, the results from the three unsteady aerodynamic tools were benchmarked against one another. With the purpose

of quantifying the effect of kite deformation, a new deflected geometry was designed. The aerodynamic results of the new and the nominal kites were compared with experiments in Section 5. Finally, Section 6 presents the main conclusions and proposes future works to improve our understanding of the aerodynamic and aeroelastic behavior of RFD kites for AWE applications.

2 | Experimental Evidence of Dynamic Stall

The estimation before modeling technique was employed in a previous work to experimentally reconstruct the state vector of the two-line RFD kite shown in Figure 1 (see physical characteristics in Table 1) during multiple figure-of-eight trajectories [36]. The commercial semirigid delta kite (HQ Fazer XXL) consists of a frame made of carbon fiber bars, a textile canopy and a bridle system with three lines per side attached to two tethers. The tethers had a fixed length of 40 m and the bridle geometry was fixed. Therefore, neither tether reel-in/reel-out nor active pitch control was applied during the flight testing but only lateral steering of the kite with the purpose of aerodynamic characterization. The reconstructed state vector included the aerodynamic velocity vector (magnitude or relative inflow speed V_A, angle of attack α and sideslip angle β) and the force and moment aerodynamic coefficients, among others.

In the following, the aerodynamic force (drag C_D, lateral C_Y and lift C_L) and moment coefficients (roll C_l, pitch C_m and yaw C_n) about the kite center of gravity (CG) are defined as

$$(C_D, C_Y, C_L) = -\frac{2}{\rho V_A^2 S} \boldsymbol{F} \cdot (\boldsymbol{i}_W, -\boldsymbol{j}_W, \boldsymbol{k}_W), \quad (1)$$

$$(C_l, C_m, C_n) = \frac{2}{\rho V_A^2 S} \boldsymbol{M} \cdot \left(\frac{\boldsymbol{i}_B}{b}, \frac{\boldsymbol{j}_B}{c}, \frac{\boldsymbol{k}_B}{b}\right), \quad (2)$$

where ρ is the air density, S, c and b are the planform area, chord and span of the kite, respectively (Table 1), $\boldsymbol{F}$ and $\boldsymbol{M}$ are the total aerodynamic force and moment vectors, and $(\boldsymbol{i}, \boldsymbol{j}, \boldsymbol{k})$ denote a Cartesian vector base. The body frame is denoted by subscript B and has the origin at the kite CG, the x_B-axis along the central bar of the kite, the z_B-axis normal to the x_B-axis, contained in the
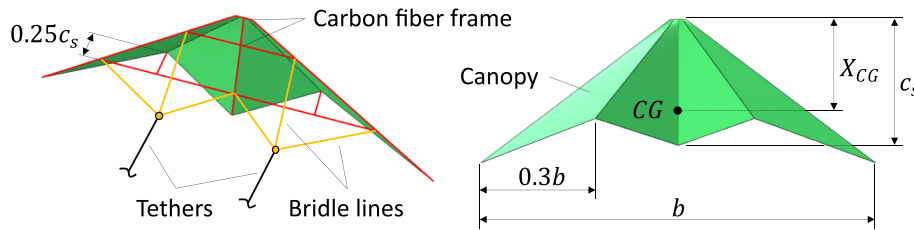
FIGURE 1 | Geometry and main components of the RFD kite (HQ Fazer XXL) with b, c_s and X_{CG} in Table 1. The carbon fiber frame, bridle lines and tethers are highlighted in red, orange and black, respectively.

TABLE 1 | Physical characteristics of the RFD kite.

Surface (S)	Span (b)	Mean aerodynamic chord (c)	Central bar chord (c_s)	Center of gravity (X_{CG})
1.86 m²	3.60 m	0.59 m	1.16 m	0.71 m

Note: The position of the center of gravity X_{CG} was measured from the nose along the central bar of the kite.

plane of symmetry of the kite and pointing toward the ground in horizontal straight flight, and the y_B-axis completes the right-handed frame. For convenience, the wind frame (denoted by W), also known as aerodynamic or apparent wind frame, is defined with the origin at the kite CG, x_W-axis along the aerodynamic velocity vector, z_W-axis normal to x_W-axis, contained in the kite symmetry plane and pointing toward the ground in horizontal straight flight, and y_W-axis completing the right-handed frame. As shown in Castro-Fernández et al. [20], the angle between the zero-lift line and the x_B-axis of the RFD kite is about 15°.

Figure 2a,b show the experimental lift C_L and drag C_D coefficients versus the angle of attack of the RFD kite during one and a half figures of eight. Three hysteresis cycles, where the aerodynamic coefficients are not unequivocally identified by the angle of attack but they also depend on its history, are observed in panels (a) and (b), and are denoted with different markers. The arrows in panels (a) and (b) indicate the loops direction showing that the coefficients reach high values before stalling when $\dot{\alpha} > 0$. However, their values considerably decrease as $\dot{\alpha}$ changes its sign. Despite only three subsequent hysteresis cycles are shown, this cyclic behavior was observed robustly during the whole experiment that lasted for 3 min and involved more that 15 figure-of-eight maneuvers.

An analysis of the evolution of α revealed that it had a period $T \approx 5$s, which is half of the period of the figure-of-eight trajectory, and an amplitude of about 20°. To understand this behavior, panel (c) of Figure 2 shows the kite trajectory only for the first two cycles of Figure 2a,b for the sake of clarity using the same markers. The magnitude of the absolute velocity of the kite V_K is shown with color. Clearly, there are two complete cycles for each

figure-of-eight maneuver and the velocity is maximum and minimum in the straight and turning path segments, respectively. This is probably induced by the type of figures of eight (up-loop) performed in the experiments, where gravity has opposite effects in the straight and turning segments. As the aerodynamic velocity, that is, the relative inflow speed, and angle of attack are given by

$$V_A \equiv V_K - V_W,$$

$$\alpha \equiv \arctan\left(\frac{V_A \cdot k_B}{V_A \cdot i_B}\right), \tag{3}$$

and the wind velocity V_W was roughly constant in the experiment, the periodic changes in the angle of attack essentially originate from the variations of the absolute velocity of the kite. For a typical aerodynamic velocity of $V_A = 15$ m/s, the reduced angular frequency associated to the periodic variation of the angle of attack in the experiment is $k = \frac{\omega c}{2V_A} \approx 0.03$, where $\omega = 2\pi/T$. For such a reduced frequency, unsteady phenomena like dynamic stall can be induced [47–49]. On the other hand, these unsteady aerodynamic effects are expected to be reduced as the period T is increased due to, for example, tether reel-out leading to wider trajectories and lower wind speeds.

To get additional evidence of the dynamic stall, a complementary experiment to the one implemented in Borobia-Moreno et al. [36] was carried out in this work. As shown in Figure 3a,b, surface tufts were mounted and recorded by a camera located at the trailing edge (central bar). Figure 3b shows two typical snapshots for attached (top) and separated (bottom) flow when the kite was located in straight and turning segments,

(a)   (b)   (c)
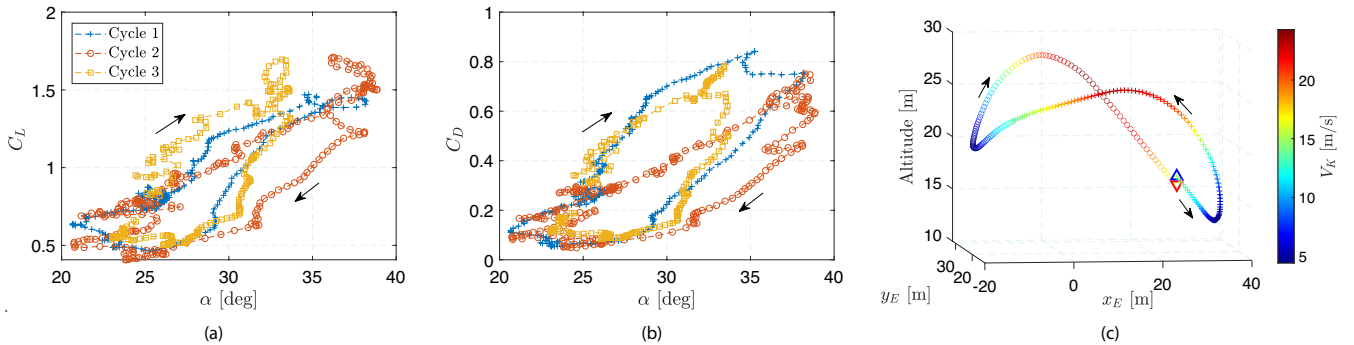
FIGURE 2 | Lift (a) and drag (b) coefficients versus the angle of attack of the RFD kite during three hysteresis cycles (one and a half figures of eight) in the experiment of Borobia-Moreno et al. [36]. Panel (c) shows the kite trajectory colored with the magnitude of the kite absolute velocity V_K. The blue upward (red downward) triangle corresponds to the start (end) of the trajectory and the crosses and circles correspond to hysteresis cycles 1 and 2 in panels (a) and (b)

(a)   (b)

FIGURE 3 | Panel (a) displays the setup of the flow visualization experiment on the RFD kite with surface tufts and an onboard camera attached to the central bar. Panel (b) shows two typical snapshots for attached (top) and separated (bottom) flow.
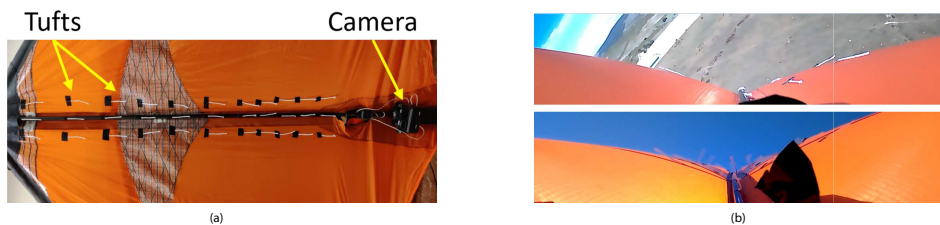
respectively. Moreover, Figure 3b shows significant variations in the shape of the kite central bar. The latter increased and decreased its curvature when the flow was attached and separated, respectively, due to the variation in aerodynamic pressure over the kite canopy, suggesting strong fluid-structure interaction. The repeated occurrence of this cyclic behavior is evident in a 6-min video available at this reference [50]. Despite experimental evidence of both dynamic stall and aerostructural deformation has been found, this work isolates the dynamic stall phenomena through aerodynamic simulation (Section 4). Additionally, a preliminary quantification of the kite deformation effects is carried out in Section 5.

Another important piece of information from the experiments, which is needed for the numerical analysis, is the kinematics of the body frame with respect to the wind frame. As the focus is on the longitudinal aerodynamic coefficients, we set the numerical tools with zero sideslip angle and the temporal profiles $V_A(t)$ and $\alpha(t)$ measured in the experiment. In fact, they were approximated by the following Fourier series with 4 harmonics,

$$
\begin{aligned}
\alpha(t) &= \alpha_{c,0} + \sum_{i=1}^{4} \alpha_{c,i} \cos(i\omega_\alpha t) + \alpha_{s,i} \sin(i\omega_\alpha t), \\
V_A(t) &= V_{Ac,0} + \sum_{i=1}^{4} V_{Ac,i} \cos(i\omega_V t) + V_{As,i} \sin(i\omega_V t),
\end{aligned}
\tag{4}
$$

to obtain a periodic and smooth kinematic input for the numerical simulations. Constants $\omega_\alpha, \omega_V, \alpha_{c,i}, \alpha_{s,i}, V_{Ac,i}$ and $V_{As,i}$, with $i = 0\ldots4$, were found by doing two fittings from the experimental results for the first two cycles (see Table 2). As shown in Figure 4, the fittings provide a good representation of the experimental results. Only the approximated kinematics of cycle 2 was prescribed in the numerical tools in Section 4.2.

TABLE 2 | Coefficients of the Fourier series fittings of Equation (4) for hysteresis cycles 1 and 2 with $i = 0\ldots4$.

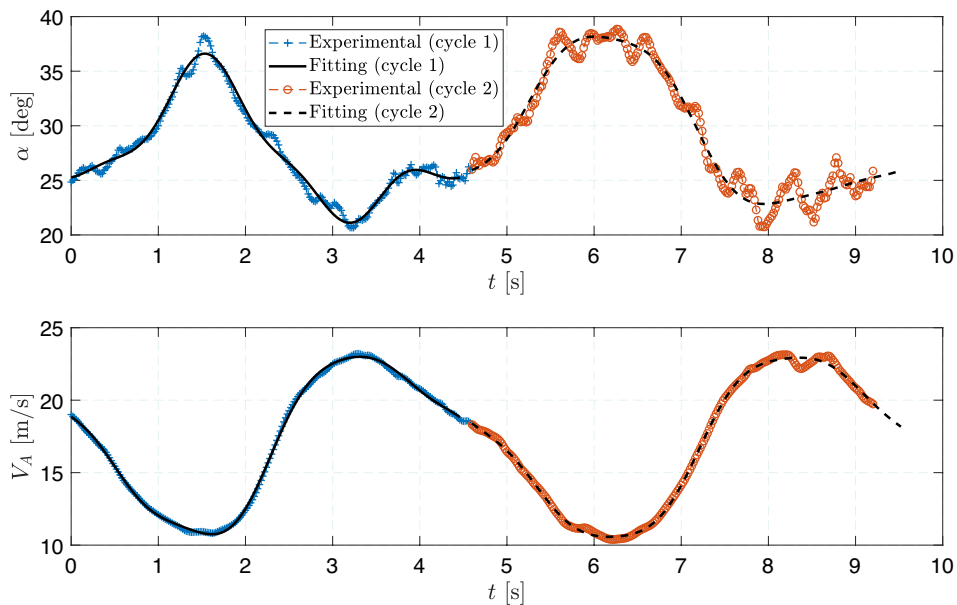|	ω_α [rad/s]	ω_V [rad/s]	$\alpha_{c,i}$ [rad]	$\alpha_{s,i}$ [rad]	$V_{Ac,i}$ [m/s]	$V_{As,i}$ [m/s]
Cycle 1	1.406	1.411	0.4817	0	17.15	0
			−0.03563	0.08705	1.561	−5.84
			−0.000265	−0.04686	−0.1326	1.129
			0.006644	−0.005468	0.2246	−0.1846
			−0.01153	0.01131	0.04555	0.2914
Cycle 2	1.276	1.29	0.515	0	16.97	0
			−0.03943	0.1281	1.827	−5.995
			−0.01586	−0.02988	−0.2662	0.9596
			−0.01045	0.0006334	0.1144	−0.07895
			0.00347	−0.006407	−0.2453	0.2069

FIGURE 4 | Experimental and approximated (Fourier series fitting) kinematic inputs for hysteresis cycles 1 and 2 in Figure 2

3 | Computational Aerodynamic Tools

This work uses three different aerodynamic tools. For convenience, the next sections provide references that describe them completely and highlight specific aspects that are relevant for this work.

3.1 | Potential-Flow Aerodynamics

The unsteady panel method [51,52] is an in-house unsteady potential-flow tool with a low to medium level of fidelity and computational cost. As compared with Castro-Fernández et al. [20], only the wake geometry was modified in this work by changing the shedding direction based on RANS data from the tool in Section 3.2 (details are provided in Appendix A).

3.2 | Unsteady Reynolds-Averaged Navier–Stokes Aerodynamics

3.2.1 | Fluid Governing Equations

The open-source multiphysics suite SU2 [44–46] have been chosen as CFD software. Due to the relatively low Mach numbers ($M \approx 0.05$), the incompressible solver was selected. Mesh deformation during the rigid motion of the kite was treated with an arbitrary Lagrangian–Eulerian (ALE) formulation. The equations governing the fluid motion in an ALE nonconservative differential form read [53],

$$\rho \frac{\partial \boldsymbol{v}}{\partial t} + \rho \left(\left[\boldsymbol{v} - \boldsymbol{v}_\Omega \right] \cdot \nabla \right) \boldsymbol{v} = -\nabla P + \mu_{tot} \Delta \boldsymbol{v}, \quad \text{in } \Omega, t > 0,$$
$$\nabla \cdot \boldsymbol{v} = \boldsymbol{0}, \qquad\qquad\qquad \text{in } \Omega, t > 0,$$
(5)

where ρ is the fluid density, $\boldsymbol{v}$ and $\boldsymbol{v}_\Omega$ are the fluid and mesh velocity vectors, P is the static pressure, Ω represents the 3D fluid domain and μ_{tot} is the sum of the dynamic viscosity μ_{dyn}, which is assumed to satisfy Sutherland's law [54], and the turbulent viscosity μ_{turb}, which is obtained from the solution of the $k - \omega$ SST turbulence model due to Menter [55]. The latter describes the evolution of the turbulent kinetic energy k and specific dissipation ω through two additional partial differential equations.

The first and second equations in (5) are the momentum and mass conservation equations which provides four partial differential equations to solve for $\boldsymbol{v}$ and P.

Figure 6a shows the fluid domain Ω ($50 \times 40 \times 20 \text{ m}^3$) considered for symmetric-flight conditions, which contains the right semi-wing of the RFD kite and the different boundary conditions. The no-slip boundary conditions, imposing that the fluid has the velocity of the body on its surface, are applied on the kite surface, the symmetric boundary conditions apply on the symmetry plane and the characteristic-based far-field boundary conditions are applied on the rest of the domain boundaries to ensure that they fulfill the free-stream conditions.

SU2 discretizes the domain with a finite volume method. In this work, the central Lax-Friedrich scheme (0.07 dissipation factor) and a Venkatakrishnan slope limiter were used to evaluate the convective terms of Equation (5). SU2 has steady and unsteady solvers. The steady solver uses a pseudo-time iteration scheme to find the steady-state solution. The selected unsteady solver uses a second-order dual time stepping procedure where there is an outer loop for the physical time steps ($\Delta t = 0.01 \text{ s}$) and an inner loop using the pseudo-time iteration of the steady solver to converge to a solution at every physical time step.

3.2.2 | Mesh and Prescribed Kinematics Module

The boundaries of the 3D computational domain were meshed with 2D elements (quadrilaterals and triangles). A refinement region around the kite was defined on the symmetry plane (see refinement region and top view of the right semiwing in the inset of Figure 6a). The surface of the kite, that encloses a volume, was meshed with 7.1×10^4 2D elements. The 3D computational domain was meshed by using hexahedral elements within the boundary layer (2 cm of thickness), tetrahedrals in the rest of the domain and pyramids in the interfaces between hexahedrals and tetrahedrals. The height of the first boundary-layer row was set to 1×10^{-5} m fulfilling the so-called $y^+ < 2$ criterion [56]. To select the final mesh, a mesh convergence analysis was performed by varying the 2D meshes of the kite surface and refinement region. Figure 5a,b shows the lift and drag coefficients versus the number of mesh elements for steady conditions
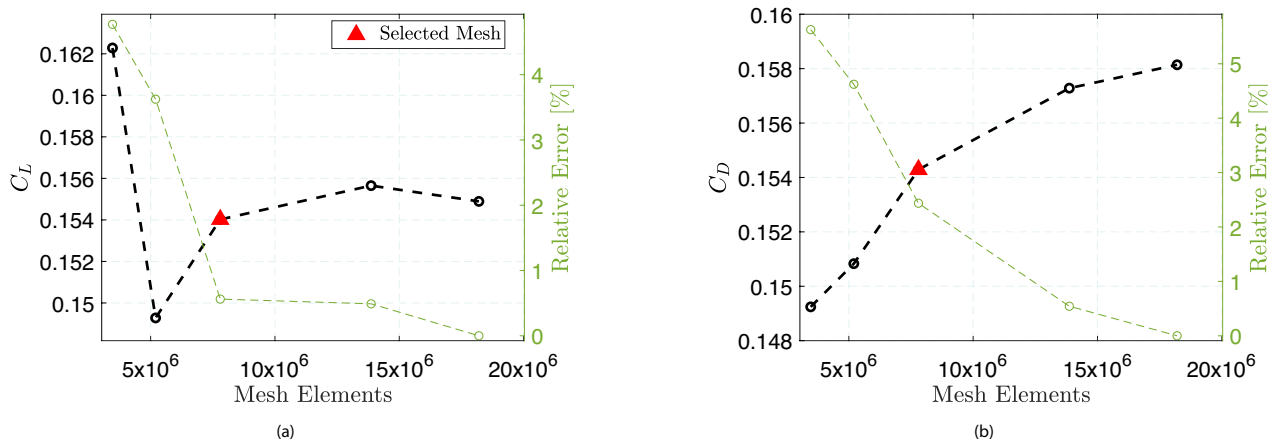
(a)

(b)

FIGURE 5 | Mesh convergence analysis for RANS computations in steady conditions with $\alpha = 20°$. Lift (a) and drag (b) coefficients (left axes) and their relative error with respect to the finest mesh considered (right axes) versus the number of mesh elements.

at $\alpha = 20°$. A mesh with roughly 7.8×10^6 3D cells was selected due to its favorable balance between computational cost and accuracy with a relative error lower than 3% as compared with the finest mesh considered.

Regarding the kite kinematics, this work employed the fluid-structure interaction framework originally developed in Fonzi et al. [57]. After minor modifications of the framework regarding rigid-body motion, it was used to prescribe the kite motion and solve for the resulting aerodynamic coefficients. In this case, two rigid-body modes are necessary to describe the kinematics between the body and wind frames. The first mode is an aerodynamic pitching motion defined as a y_B-axis rotation of the kite of value $\alpha(t)$ given by Equation (4). On the other hand, following Equation (3), the fitted aerodynamic velocity $V_A(t)$ of Equation (4) is imposed in SU2 through the following two terms:

$$\boldsymbol{V}_W = -V_{Ac,0}\boldsymbol{i}_G, \ \boldsymbol{V}_K = \frac{\mathrm{d}\boldsymbol{O}_G\boldsymbol{O}_B}{\mathrm{d}t}, \tag{6}$$

with $V_{Ac,0}$ given in Table 2 and subscript G denoting a global frame that has axes parallel to the wind frame and is at rest with respect to the domain as shown in Figure 6a. The wind velocity $\boldsymbol{V}_W$ is set as a constant free-stream velocity in SU2. The kite absolute velocity $\boldsymbol{V}_K$ is induced by a translation (second rigid-body mode) along x_G-axis as

$$\begin{aligned} \boldsymbol{O}_G\boldsymbol{O}_B(t) &= \int_0^t \boldsymbol{V}_K(t)\mathrm{d}t = \int_0^t \left[\boldsymbol{V}_A(t) + \boldsymbol{V}_W(t)\right]\mathrm{d}t \\ &= \sum_{i=1}^4 \left(\frac{V_{Ac,i}}{i\omega_V}\sin(i\omega_V t) - \frac{V_{As,i}}{i\omega_V}\cos(i\omega_V t) + \frac{V_{As,i}}{i\omega_V}\right)\boldsymbol{i}_G, \end{aligned} \tag{7}$$

with initial conditions $\boldsymbol{O}_G\boldsymbol{O}_B(0) = \boldsymbol{0}$.

The framework needs a set of structural nodes which in this case are coincident with the aerodynamic nodes of the kite surface mesh. After prescribing the position of the structural nodes following the two rigid-body modes, the fluid mesh must be deformed around the kite surface mesh. To do this, the framework

calls a dedicated SU2 mesh deformation solver based on a linear elasticity analogy. Finally, the incompressible unsteady RANS solver of SU2 solves the fluid equations providing the aerodynamic coefficients at the current time step as an output. The loop continues by prescribing the positions of the structural nodes at the next physical time step.

3.3 | Semiempirical Dynamic Stall Aerodynamic Model

The third aerodynamic method is a semiempirical dynamic stall model based on the original Leishman–Beddoes model [38] after some of the modifications described in Hansen et al. [41] and Boutet et al. [42]. They consider unsteady effects in the aerodynamic coefficients as variations about the steady counterparts, and adapt the traditional formulas to low Reynolds and low Mach numbers, respectively. The Leishman–Beddoes model and its variants were routinely used to model dynamic stall in 2D airfoils [39,40], and in some cases, they were applied to several spanwise wing sections integrating the individual contributions to obtain the global aerodynamic coefficients. In this work, the model is applied directly to the aerodynamic coefficients of the RFD kite and the typical section for 2D computations will be the central bar that is considered a flat plate with chord $c_s = 1.16$ m. Figure 6b displays a sketch of such a typical section with the center of pressure (CP) at a distance gc_s from the quarter-chord, the separation point (SP) at a distance fc_s from the leading edge and the kite CG at a distance X_{CG} from the leading edge.

The proposed semiempirical model combines attached-flow theory (numerical part) through the 3D potential-flow model UnPaM (Section 3.1), unlike previous dynamic stall models that used 2D potential-flow theory, and a phenomenological dynamic stall module (empirical part) with three building blocks in state-space form. The free parameters of the empirical part were fined tuned by using CFD data from SU2 (Section 3.2) which is considered high-fidelity. Once the tool is calibrated
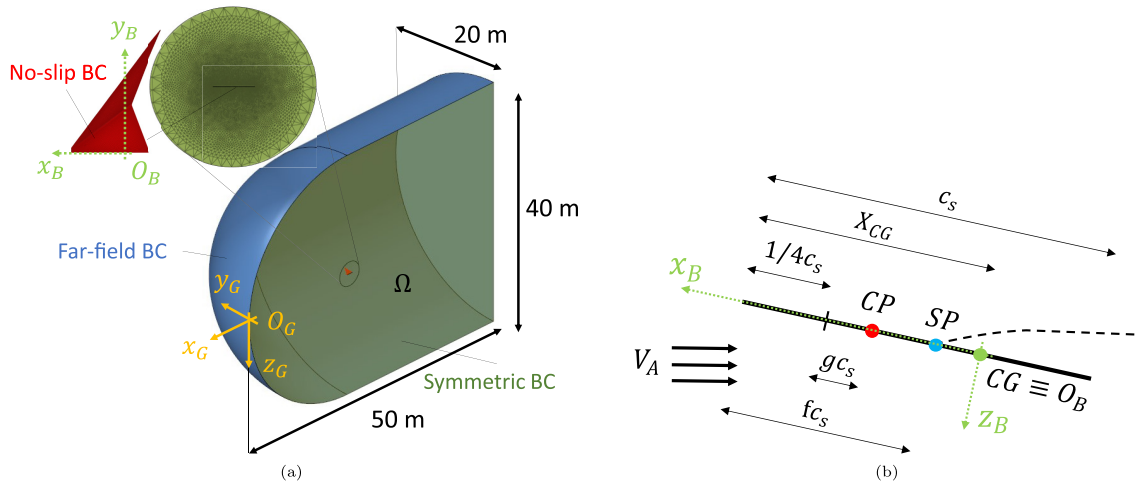
FIGURE 6 | Panel (a) shows the fluid domain Ω indicating the no-slip, symmetric (inset of the refinement region around the kite and top view of the right semiwing of the RFD kite) and far-field boundary conditions (denoted by BC), and the global reference frame (denoted by subscript G). Panel (b) shows a sketch of the typical section (kite central bar) used by the semiempirical dynamic stall model with the center of pressure (CP), separation point (SP) and center of gravity (CG).

for the RFD kite, the main three-dimensional and dynamic stall effects are modeled at a much lower computational cost than CFD.

3.3.1 | State-Space Equations

The three phenomenological dynamic stall blocks, namely, leading-edge separation, trailing-edge separation and leading-edge vortex, model the main physical phenomena associated to dynamic stall [38,42]. They are governed by a set of three first-order ordinary differential equations for the state $\boldsymbol{x}$ and an output model for the space $\boldsymbol{y}$,

$$
\begin{aligned}
\dot{\boldsymbol{x}} &= \boldsymbol{F}(\boldsymbol{x}, \boldsymbol{u}, \boldsymbol{C}^P, \boldsymbol{\theta}), \\
\boldsymbol{y} &= \boldsymbol{G}(\boldsymbol{x}, \boldsymbol{u}, \boldsymbol{C}^P, \boldsymbol{\theta}),
\end{aligned}
\tag{8}
$$

with $\dot{\boldsymbol{x}}$ the time derivative of $\boldsymbol{x}$. The state $\boldsymbol{x}$, space $\boldsymbol{y}$, kinematic input $\boldsymbol{u}$, potential-flow coefficients $\boldsymbol{C}^P$ and parameters $\boldsymbol{\theta}$ vectors are given by

$$
\begin{cases}
\boldsymbol{x} = [\overline{\alpha}', f', C_L^v]^\top, \\
\boldsymbol{y} = [C_D^{DS}, C_Y^{DS}, C_L^{DS}, C_l^{DS}, C_m^{DS}, C_n^{DS}]^\top, \\
\boldsymbol{u} = [\alpha, V_A]^\top, \\
\boldsymbol{C}^P = [C_D^P, C_Y^P, C_L^P, C_l^P, C_m^P, C_n^P]^\top, \ \boldsymbol{C}_j^P = \left[C_j^{P,S}, C_j^{P,Dc}, C_j^{P,Di}\right], \ j = D, Y, L, l, m, n, \\
\boldsymbol{\theta} = [\boldsymbol{\theta}^S, \boldsymbol{\theta}^D]^\top, \ \boldsymbol{\theta}^S = [a_{DS}, b_{DS}, c_{DS}, B_1, B_2, C_{D0}^{CFD,S}, C_{m0}^{CFD,S}], \ \boldsymbol{\theta}^D = [T_f, T_v, T_{vl}].
\end{cases}
\tag{9}
$$

State $\overline{\alpha}'$ is a delayed version of the effective angle of attack $\overline{\alpha}$, defined from the normal (V_N) and chordwise (V_C) velocities induced at the quarter-chord as

$$
\overline{\alpha} = \arctan\left(\left.\frac{V_N}{V_C}\right|_{1/4 c_s}\right) = \arctan\left(\frac{V_A \sin\alpha - c_s[a - 1/4]\dot{\alpha}}{V_A \cos\alpha}\right),
\tag{10}
$$

with $a \equiv X_{CG}/c_s$ (see Figure 6b). The state variable f' is the delayed trailing-edge separation point location f in the typical section of Figure 6b (f is 0 for fully separated flow and 1 for fully attached flow), and C_L^v is the lift contribution due to the change of circulation caused by the oscillatory motion. The space vector $\boldsymbol{y}$ contains the six aerodynamic coefficients obtained with the semiempirical dynamic stall model. The kinematic input $\boldsymbol{u}$ of the dynamic stall model has two components: the angle of attack α and the aerodynamic velocity V_A. Vector $\boldsymbol{C}^P$ contains the potential-flow aerodynamic coefficients with superscript S standing for steady, and Dc and Di for dynamic circulatory and impulsive or added mass components, respectively. The vector of parameters $\boldsymbol{\theta}$ gathers static $\boldsymbol{\theta}^S$ and dynamic $\boldsymbol{\theta}^D$ parameters. The static ones, which were taken from Boutet et al. [42] and steady RANS data from SU2, are shown in Table 3. The dynamic parameters consist of three time delays that were fine-tuned by using unsteady RANS data from SU2. The final values are shown in Table 3. For the sake of clarity, further details of the state-space Equation (8) are provided in Appendix B.

In an aerodynamic simulation with the semiempirical dynamic stall tool, the kinematic inputs given by Equation (4) are first prescribed into UnPaM to obtain the potential-flow steady and dynamic (split into circulatory and impulsive) coefficients $\boldsymbol{C}^P$ at every time step. Known $\boldsymbol{u}$, $\boldsymbol{C}^P$ and $\boldsymbol{\theta}$, the state-space Eqs. 8 are run with a set of initial conditions that are irrelevant for our analysis (e.g., $\boldsymbol{x} = [0.1, 0.1, 0.1]$) until a stable periodic solution is reached. The six aerodynamic coefficients contained in $\boldsymbol{y}$ resulting from the semiempirical model at every time step are obtained as an output. An important remark is that the coupling between UnPaM and the state-space equations is one-way because only the inputs by UnPaM ($\boldsymbol{C}^P$) are considered in the state-space system. Consequently, the phenomenological dynamic stall module modify the 3D potential-flow aerodynamic coefficients of the RFD kite considering dynamic stall phenomena that include leading-edge separation delays, lagged trailing-edge separation and changes in circulation as explained in Appendix B.

4 | Results

4.1 | Aerodynamic Results for Steady Conditions

Before discussing the unsteady results of the three aerodynamic tools under unsteady kinematic conditions, a comparison between potential-flow (UnPaM) and RANS (SU2) results for steady conditions (fixed aerodynamic velocity and angle of attack) is shown in this section. Figure 7 shows the three longitudinal aerodynamic coefficients (lift, drag and pitch moment) versus the angle of attack. The comparison between potential flow and RANS in the lift coefficient versus the angle of attack curve (Figure 7a) shows that both approximations have slightly different slopes. UnPaM overestimates the lift coefficient because it does not consider recirculation bubbles and separation in the complex geometry of the RFD kite. Moreover, the potential-flow curve keeps linear for the full range of α while RANS computations predict stall occurrence for $\alpha > 36$ deg. However, both tools predict approximately the same zero-lift angle of attack (~ 16 deg). Regarding the curve of the drag coefficient versus angle of attack (Figure 7b), UnPaM inherently underestimates the drag coefficient due to the lack of viscosity. The effect is more remarkable for high values of α where separation becomes more important. The RANS C_D versus α follows a typical polar shape with the minimum around the zero-lift angle of attack. The pitch moment coefficient as a function of α (Figure 7c) shows a good agreement between potential flow and RANS computations for a large range of angles of attack except in the stall region, where UnPaM does not predict the sudden decrease in C_m after stall.

A local analysis of the kite steady aerodynamics by monitoring the pressure coefficient C_p on the kite surface at a mild angle of attack (25°) is shown in Figure 8. Subpicture (a) shows the C_p distribution on the kite upper surface and four spanwise sections of the right semiwing at distances $0, 0.25, 0.5,$ and 1 m from the kite

TABLE 3 | Static θ^S and dynamic θ^D parameters of the dynamic stall model.

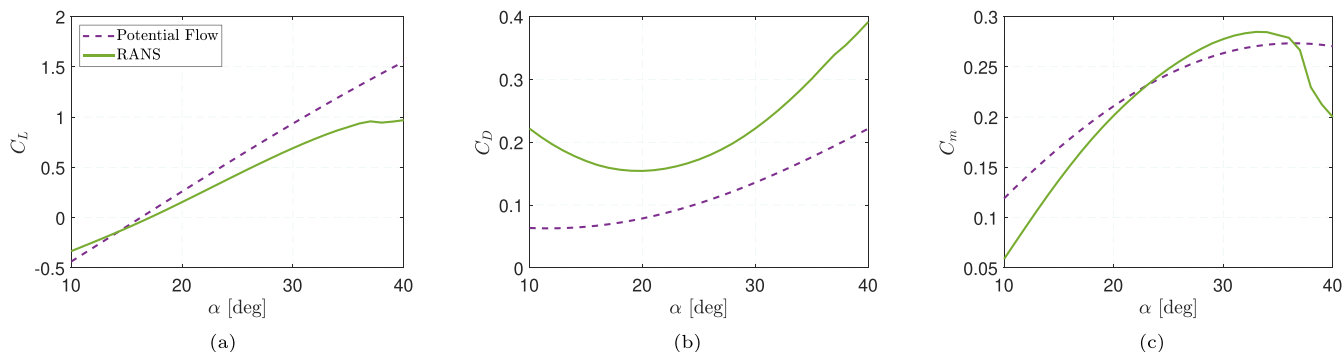| a_{DS}	b_{DS}	c_{DS}	B_1	B_2	$C_{D0}^{CFD,S}$	$C_{m0}^{CFD,S}$	T_f	T_v	T_{vl}
-2.97×10^{-5}	3.50×10^{-3}	-2.59×10^{-2}	1.50×10^{-2}	7.50×10^{-2}	0.17	0.08	0.06	0.10	0.26

FIGURE 7 | Lift (a), drag (b), and pitch moment (c) coefficients versus the angle of attack of the RFD kite in steady conditions.
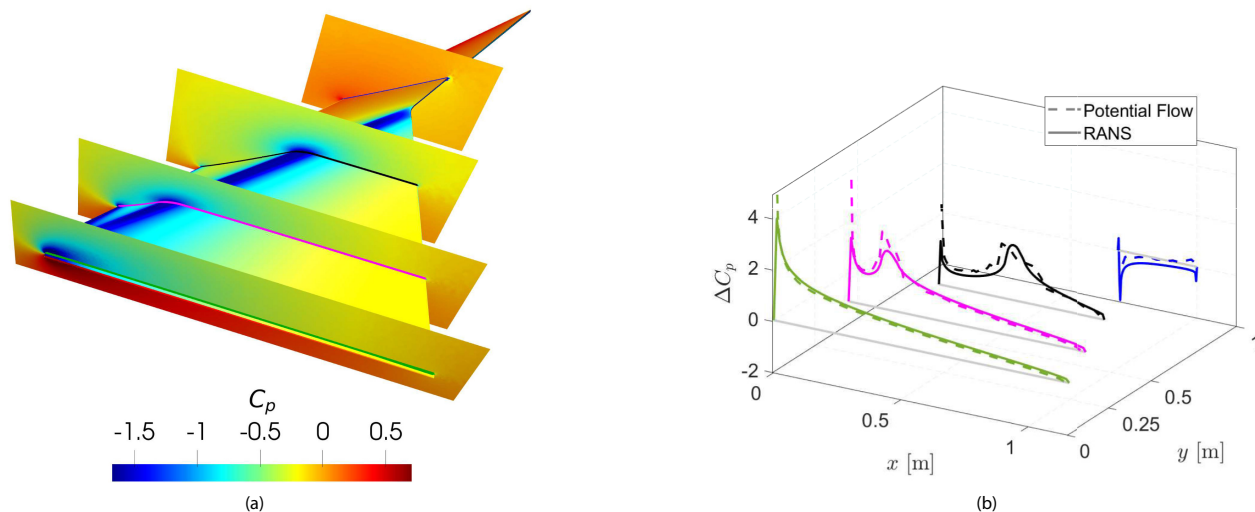

FIGURE 8 | Steady RANS simulation of the RFD right semiwing at an angle of attack of 25°. Panel (a) shows the pressure coefficient C_p distribution on the kite extrados and four spanwise sections at distances $y = 0, 0.25, 0.5, 1\,\mathrm{m}$ from the kite symmetry plane. Panel (b) shows a comparison between potential flow and RANS of the pressure coefficient difference between the intrados and extrados ΔC_p along the chord x of the four spanwise sections in panel (a)

symmetry plane. A negative-pressure region (suction) is found along the joint between the kite planes at different dihedral angles. In this region, a recirculation bubble forms even at low angles of attack, and it bursts at high α being responsible for the full separation of the extrados of the wing. Subpicture (b) shows the pressure coefficient difference between the intrados (pressure side) and extrados (suction side) ΔC_p of the kite for the spanwise sections in panel (a) computed with potential flow (dashed lines) and RANS (solid lines). Both tools qualitatively agree on the distribution of ΔC_p of the four sections. Nevertheless, UnPaM predicts higher suction peaks in the leading edge and the joint between the planes at different dihedrals. Moreover, near the wing tip (section $y = 1\,\mathrm{m}$), RANS computations predict a more negative ΔC_p that leads to a higher downward force. Due to these effects, UnPaM generally overestimates the lift coefficient as compared with RANS as shown in Figure 7a.

4.2 | Aerodynamic Results for Unsteady Conditions

Unsteady kinematic conditions were prescribed in the three aerodynamic tools described in Section 3 and the results were

compared. Pitching motion ($\dot{\alpha} \neq 0$) and pitching motion with unsteady aerodynamic velocity ($\dot{\alpha} \neq 0$ and $\dot{V}_A \neq 0$) were tested to discuss the main drivers of the dynamic phenomena.

4.2.1 | Aerodynamic Results for Pitching Motion

The periodic pitching motion ($\dot{\alpha} \neq 0$) of cycle 2 in Figure 4 was firstly tested. The pressure coefficient C_p on the kite surface and some streamlines (colored with a gray scale) computed with unsteady RANS are shown in panels (a)–(f) of Figure 9 for different instants during the pitching motion: $\alpha = 23°$ (upstroke), 30° (upstroke), 35° (upstroke), 38° (downstroke), 35° (downstroke), and 30° (downstroke), where upstroke and downstroke indicate $\dot{\alpha} > 0$ and $\dot{\alpha} < 0$, respectively. It is observed that during the upstroke at low angles of attack (a), narrow negative-pressure (suction) regions are present in the two diagonal lines joining the planes of the kite at different dihedral angles. However, the flow is fully attached. As the angle of attack increases (b, c), wider negative-pressure regions appear near the kite nose and a leading-edge vortex starts forming (see vortex-like streamlines near the kite nose in panels (b) and (c)). The colored streamlines show that there
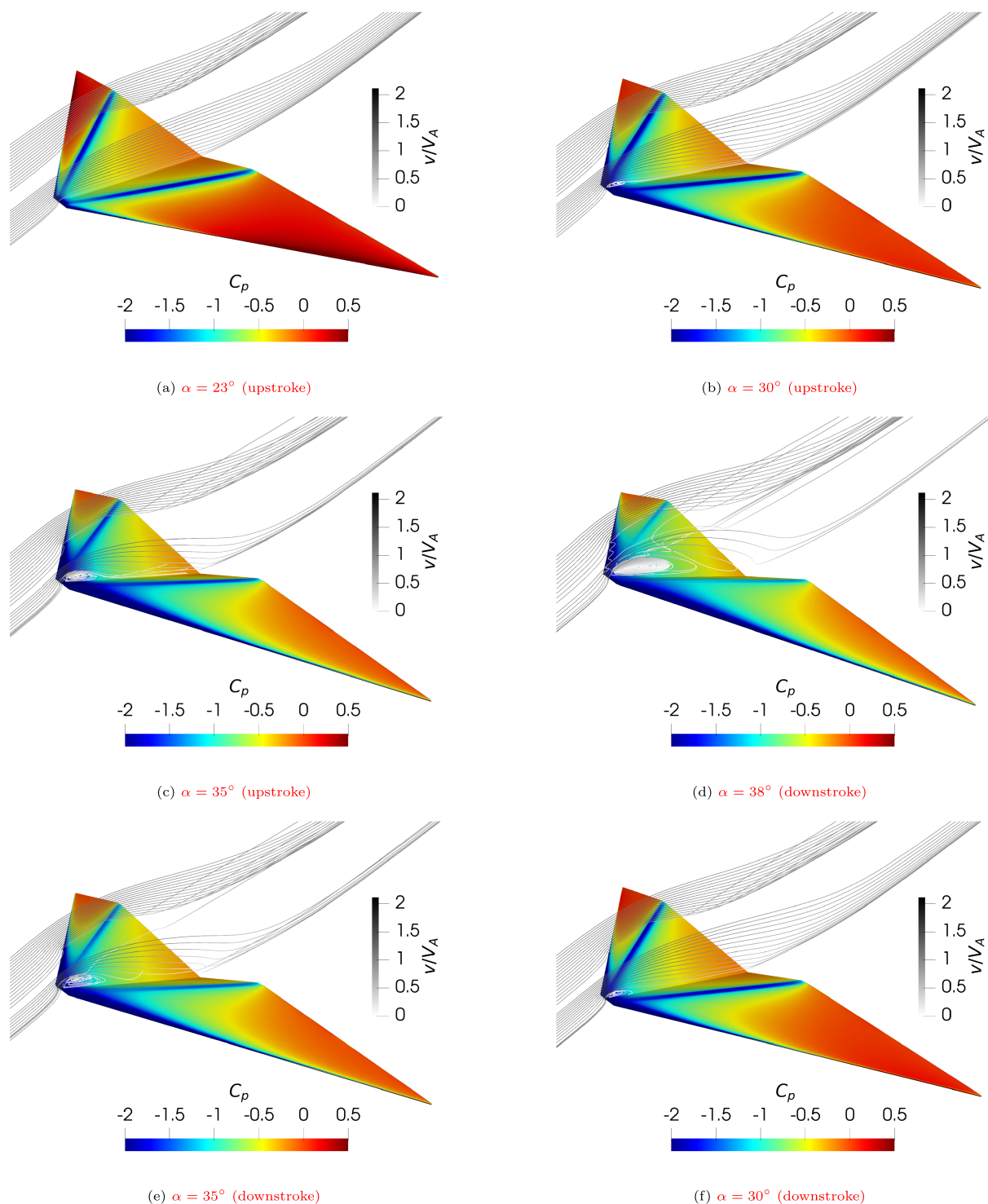
(a) $\alpha = 23°$ (upstroke)

(b) $\alpha = 30°$ (upstroke)

(c) $\alpha = 35°$ (upstroke)

(d) $\alpha = 38°$ (downstroke)

(e) $\alpha = 35°$ (downstroke)

(f) $\alpha = 30°$ (downstroke)

FIGURE 9 | Unsteady RANS simulation for the pitching motion ($\dot{\alpha} \neq 0$) of cycle 2 in Figure 4. Panels (a)-(f) correspond to angles of attack of 23° (upstroke), 30° (upstroke), 35° (upstroke), 38° (downstroke), 35° (downstroke), and 30° (downstroke), respectively. The streamlines are colored with the normalized velocity (local velocity over aerodynamic velocity)

is a notable reduction of velocity within the vortex as compared with the rest of the fluid flow, that is, a low-pressure region. Nearly at the highest angle of attack (d), the leading-edge vortex detaches triggering flow separation on most of the kite extrados. Finally, during the downstroke (e, f), the flow gradually reattaches at low-enough angles of attack. This behavior is observed cyclically due to the periodicity of the prescribed pitching kinematics. A complementary analysis to

identify and track vortical structures was performed by using iso-contours of Q, that is, the second invariant of the velocity gradient tensor, similarly to the literature [58] and [59]. It revealed that the size of the leading-edge vortex becomes apparent and starts growing from $t/T \simeq 0.39$, with $t/T = 0$ for $\alpha = 23°$, and is shed at $t/T \simeq 0.53$. Prior to this fast growth, a small leading-edge vortex with a virtually fixed size remains attached to the leading edge.

Figure 10 shows the lift and drag coefficients versus α computed by the three tools for the pitching kinematics. To help interpret the unsteady results, the steady curves computed with RANS (denoted by RANS (steady)) are also shown. Results show a hysteresis on the aerodynamic coefficient response, which does not only depend on the instantaneous angle of attack but also on its history. Regarding the lift coefficient versus the angle of attack (Figure 10a), the unsteady RANS (denoted by URANS) and semiempirical dynamic stall (denoted by Dynamic Stall) tools provide very similar outputs, verifying the second tool against URANS. During the upstroke, the lift coefficient is higher than in the steady case because the boundary layer is energized by the pith-up motion preventing separation. The downstroke is characterized by a lower C_L due to the full separation triggered by the detachment of the recirculation bubble (Figure 9d). The potential-flow tool (denoted by Potential Flow) presents a hysteresis cycle distanced from and in opposite direction to the ones predicted by the other two tools. Such big differences are due to the distinct nature of the potential-flow hysteresis. The latter is due to the change in aerodynamic normal wash on the kite surface induced by the pitching motion and the unsteady aerodynamic lags instead of viscous effects.

A remarkable match between the URANS and dynamic stall models is observed in the C_D versus α curves (Figure 10b). Similarly to the $C_L(\alpha)$ curve, the C_D is higher during the upstroke than during the downstroke for the unsteady RANS and Dynamic Stall models. This is because the induced drag increases as a consequence of the increase in lift. The potential-flow curve presents negligible hysteresis and lower values than the other tools which can be explained by the lack of viscous effects (wall friction and separation). An analysis of the relative errors among the three aerodynamic tools is addressed in Appendix C. The average error in C_L and C_D between potential flow and unsteady RANS is about 40% while that for the semiempirical dynamic stall model is lower than 5%.

4.2.2 | Comparison Between Pitching Motion and Pitching Motion With Unsteady Aerodynamic Velocity

The pitching motion ($\dot{\alpha} \neq 0$) and unsteady aerodynamic velocity ($\dot{V}_A \neq 0$) of cycle 2 in Figure 4 were prescribed in the unsteady RANS tool. Figure 11 shows the lift and drag coefficients as a
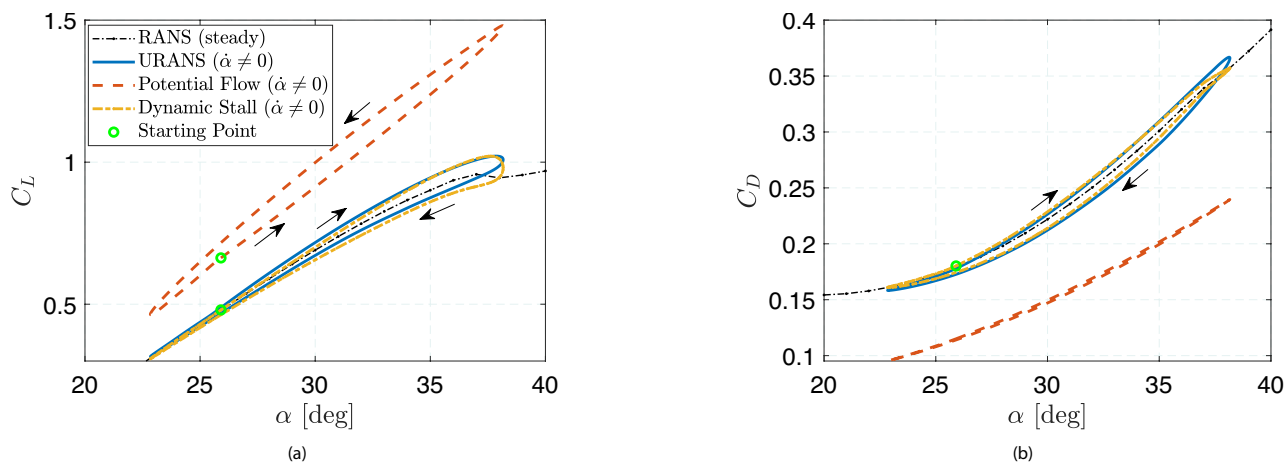

FIGURE 10 | Lift (a) and drag (b) coefficients versus the angle of attack of the RFD kite for the pitching motion of cycle 2 in Figure 4. Results from steady RANS, unsteady RANS, potential flow and semiempirical dynamic stall models are shown.
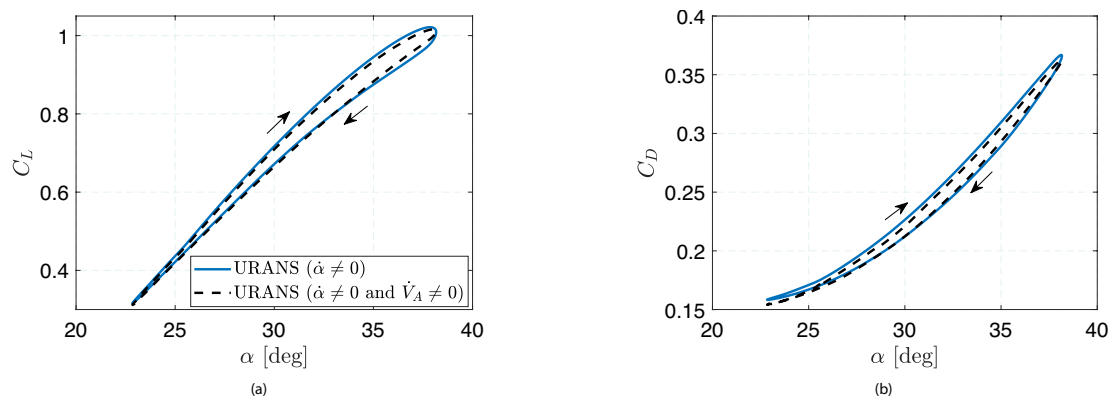

FIGURE 11 | Lift (a) and drag (b) coefficients versus the angle of attack of the RFD kite. Results from unsteady RANS under conditions i) $\dot{\alpha} \neq 0$ and ii) $\dot{\alpha} \neq 0$ and $\dot{V}_A \neq 0$ of cycle 2 in Figure 4 are shown.
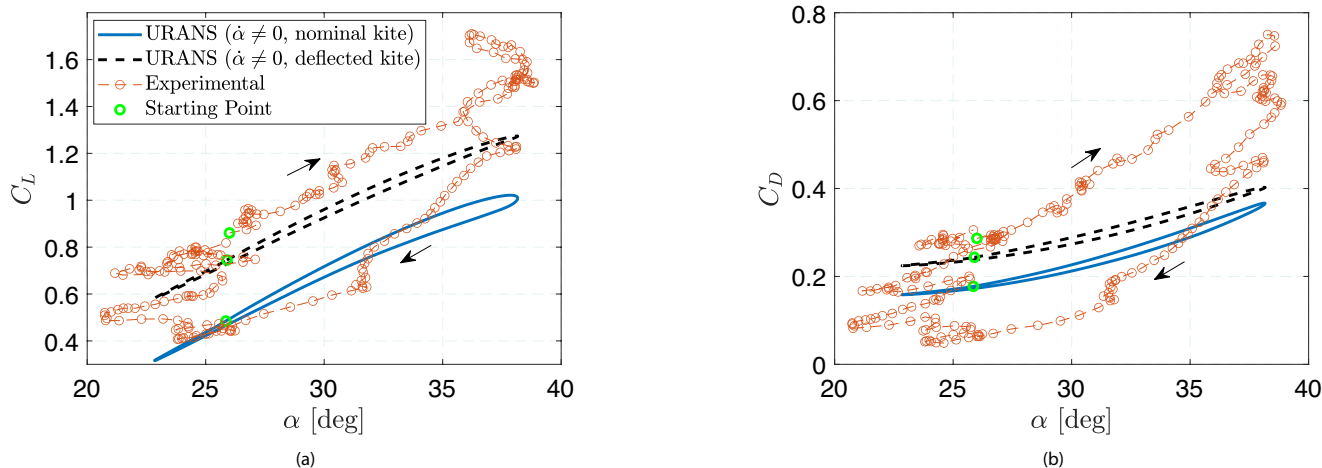
FIGURE 12 | Lift (a) and drag (b) coefficients versus the angle of attack of the RFD kite for the pitching motion of cycle 2 in Figure 4. Results from unsteady RANS of the nominal and deflected kites, and experimental data from Borobia-Moreno et al. [36] are shown.

function of the angle of attack computed with unsteady RANS for conditions $\dot{\alpha} \neq 0$ and $\dot{V}_A \neq 0$ as compared with pitching-only conditions $\dot{\alpha} \neq 0$. The main motivation for the comparison of the two URANS simulations is to check the effects of a nonconstant reduced frequency of the pitching motion and the added mass (impulsive) aerodynamic forces. The numerical tool predicts very similar hysteresis loops for both sets of kinematic conditions. Therefore, conditions $\dot{V}_A \neq 0$ do not essentially affect the dynamic stall phenomenon being the pitching motion its main driver.

5 | Discussion

The comparison of the experimental results and the unsteady aerodynamic simulations revealed some important facts. The RANS simulations showed that the cyclic flow separation observed in the experiments (see Figure 3b and full video in this reference [50]) is driven by the periodic changes in the angle of attack. The simulations demonstrated that a leading-edge vortex forms and detaches cyclically triggering full flow separation on the kite extrados. An analysis of Figures 2a,b and 10a,b reveals that the evolution of the lift and drag coefficients during a cycle is qualitatively captured by the unsteady aerodynamic tools and the experimental and numerical results agree in terms of direction of the hysteresis loops.

However, as shown by Figure 12a, there may be additional phenomena playing an important role during the figure-of-eight maneuvers. The amplitude of the experimental cycles for the lift coefficient (dashed orange line with markers) can reach almost 100%, while the RANS simulations (blue line) predicts that dynamic stall is responsible for only about 15-20%.

The important kite deformation observed in the experiments (see video in this reference [50]) suggests that aeroelastic phenomena may work collaboratively with the dynamic stall to produce high-amplitude cycles. Moreover, the RANS simulations captures very well the lower part of the cycle, where the aerodynamic loads are smaller and the kite geometry may be closer

to the one used in the RANS simulations (kite geometry without any aerodynamic load).

Although a coupled fluid-structure interaction analysis is beyond the scope of this work, an extra campaign of simulations has been carried out considering a different shape of the kite (deflected shape), selected taking inspiration from the images of the experimental activity; in particular, it was decided to keep the same geometry for the outer edges of the kite and introduce a deflection (curvature) of 5% at their middle points for the central bar and the two diagonal lines joining the two planes at different dihedrals. A new fluid mesh was generated for the new geometry and the kite was considered as rigid for the subsequent aerodynamic simulations.

The black dashed line in Figure 12a,b shows the lift and drag coefficients of the deflected kite versus α computed with unsteady RANS for pitching conditions ($\dot{\alpha} \neq 0$). Regarding the $C_L(\alpha)$, the numerical hysteresis cycles of the deflected kite fits well the upper branch of the experimental results. In the case of the $C_D(\alpha)$, this match is moderate as the experimental drag coefficient, estimated through the estimation before modeling technique in Borobia-Moreno et al. [36], incorrectly attributed the drag of the two tethers to the kite. Additionally, the amplitude of the cycle is smaller for the deformed kite due to the delay of flow separation induced by the new shape. A detailed analysis revealed that, unlike for the original geometry, the flow is not fully separated at the maximum angle of attack of the pitching motion (Figure 9d). Two conclusions can be drawn: the amplitude of the cycles observed experimentally is due in major measure to the aero-structural coupling, that is, the kite changing its shape. However, unsteady aerodynamic phenomena (dynamic stall) are present and play a role, as suggested in Borobia-Moreno et al. [36] and corroborated by this work.

6 | Conclusions

A detailed investigation of the unsteady aerodynamics of delta kites applied to AWE during typical figure-of-eight maneuvers

has been performed by combining experiments and simulations. In the first place, experimental evidences of the behavior of delta kites were shown. The post-processing of experimental data from a flight test campaign revealed strong and persistent hysteresis in the lift and drag coefficients versus the angle of attack. Moreover, an in-situ flow visualization showed periodic separation and reattachment of the flow and significant deformations of the kite structure. Dynamic stall, driven by periodic changes in the angle of attack with amplitudes and periods of about 20° and 5s, was identified as one of the relevant unsteady phenomena involved. To allow for a deep understanding and characterization of the dynamic stall behavior, three unsteady computational aerodynamic tools were benchmarked against one another and the experimental data. The level of fidelity and computational cost ranged from low for the potential-flow tool (UnPaM) to high for RANS (SU2). Moreover, aiming at reducing the computational burden while keeping a high accuracy, a semiempirical dynamic stall model was proposed.

The comparison between UnPaM and SU2 results for steady conditions, that is, fixed aerodynamic velocity and angle of attack, showed that viscous effects such as recirculation bubbles, separation and wall friction, not modeled in the in-house panel method, induce moderate discrepancies in the lift and drag responses, most relevant at higher angles of attack where separation dominates. However, both tools agreed on the order of magnitude and trend of the pitch moment coefficient before stall. A local analysis of the pressure coefficient difference between the intrados and extrados ΔC_p demonstrated that despite the qualitative agreement between both tools was very good, UnPaM predicted higher suction peaks in the leading edge and the joint between the planes at different dihedral angles. This essentially leads to an overestimation of the lift coefficient by the potential-flow tool.

The unsteady aerodynamic simulations of the three tools allowed to isolate and quantify the dynamic stall phenomenon by prescribing the kite kinematics measured in the experiments. The pitching motion ($\dot{\alpha} \neq 0$) without the need of including an unsteady aerodynamic velocity ($\dot{V}_A \neq 0$) demonstrated to be the main driver of dynamic stall. The results from unsteady RANS partially explained the experimental hysteresis in the lift and drag coefficients versus the angle of attack. Analogously to the experimental observations, a leading-edge vortex that periodically forms and detaches was identified in the unsteady RANS simulations. A comparison of the three numerical tools highlighted the inability of UnPaM to capture the dynamic stall phenomenon. After fine-tuning the free parameters of the semiempirical dynamic stall tool with steady and unsteady RANS data, a remarkable agreement with unsteady RANS was achieved on the lift and drag coefficients. Therefore, the semiempirical tool becomes a low-cost but accurate aerodynamic tool that can be coupled with flight simulators. This is especially true for rigid AWE aircraft (fixed-wing, box-wing, etc.) performing highly dynamic maneuvers where unsteady aerodynamics plays a fundamental role.

Motivated by the significant structural deformations experimentally observed, a deflected kite was aerodynamically analyzed as a rigid body. The results revealed that a small imposed curvature (5%) on the kite central bar and the joint between planes at different dihedrals considerably shifted up the $C_L(\alpha)$ and $C_D(\alpha)$ curves. These last results suggest that, to fully reproduce the amplitude of the hysteretic response, fluid-structure coupling will need to be included. Future works will be conducted on aeroelastic modeling of delta kites to fully understand and characterize the phenomena involved during the flight of these semirigid kites.

Peer Review

The peer review history for this article is available at https://www.webofscience.com/api/gateway/wos/peer-review/10.1002/we.2932.

Data Availability Statement

The data that support the findings of this study are available from the corresponding author upon reasonable request.

References

1. L. Fagiano, M. Milanese, "Airborne Wind Energy: An Overview," In: Proceedings of the American Control Conference; (2012):3132-3143.

2. A. Cherubini, A. Papini, R. Vertechy, M. Fontana, "Airborne Wind Energy Systems: A Review of the Technologies," *Renewable and Sustainable Energy Reviews.* 51 (2015):1461-1476.

3. U. Fechner, R. van der Vlugt, E. Schreuder, R. Schmehl, "Dynamic Model of a Pumping Kite Power System," *Renewable Energy.* 83 (2015):705-716.

4. G. Sánchez-Arriaga, A. Pastor-rodríguez, M. Sanjurjo-rivo, R. Schmehl, "A Lagrangian Flight Simulator for Airborne Wind Energy Systems," *Applied Mathematical Modelling.* 69 (2019):665-684.

5. C. Vermillion, M. Cobb, L. Fagiano, et al., "Electricity in the Air: Insights From Two Decades of Advanced Control Research and Experimental Flight Testing of Airborne Wind Energy Systems," *Annual Review of Control.* 52 (2021):330-357.

6. U. Fasel, P. Tiso, D. Keidel, G. Molinari, P. Ermanni, "Reduced-Order Dynamic Model of a Morphing Airborne Wind Energy Aircraft," *AIAA Journal.* 57, no. 8 (2019):3586-3598.

7. N. Pynaert, T. Haas, J. Wauters, G. Crevecoeur, J. Degroote, "Wing Deformation of an Airborne Wind Energy System in Crosswind Flight Using High-Fidelity Fluid–Structure Interaction," *Energies.* 16, no. 2 (2023):602.

8. M. L. Loyd, "Crosswind Kite Power," *Journal of Energy.* 4, no. 3 (1980):106-111.

9. J. Wijnja, R. Schmehl, R. D. Breuker, K. Jensen, D. V. Lind, "Aeroelastic Analysis of a Large Airborne Wind Turbine," *Journal of Guidance, Control, and Dynamics.* 41 (2018):1-12.

10. R. Leloup, K. Roncin, G. Bles, J. Leroux, "Estimation of the Lift-to-Drag Ratio Using the Lifting Line Method: Application to a Leading Edge Inflatable Kite," *Airborne Wind Energy. Ser. Green Energy Technol.* Berlin Heidelberg: Springer; (2013):339-355.

11. T. Haas, J. De Schutter, M. Diehl, J. Meyers, "Large-Eddy Simulation of Airborne Wind Energy Farms," *Wind Energy Science.* 7, no. 3 (2022):1093-1135.

12. R. Damiani, F. Wendt, J. Jonkman, J. Sicard, "A Vortex Step Method for Nonlinear Airfoil Polar Data as Implemented in KiteAeroDyn," In: AIAA Scitech 2019 Forum; (2019):804.

13. A. A. Candade, M. Ranneberg, R. Schmehl, "Structural Analysis and Optimization of a Tethered Swept Wing for Airborne Wind Energy Generation," *Wind Energy*. 23, no. 4 (2020):1006-1025.

14. O. Cayon, M. Gaunaa, R. Schmehl, "Fast Aero-Structural Model of a Leading-Edge Inflatable Kite," *Energies*. 16, no. 7 (2023):3061.

15. M. Gaunaa, F. P.P. Carqueija, P.-E. Réthoré, N. N. Sørensen, "A Computationally Efficient Method for Determining the Aerodynamic Performance of Kites for Wind Energy Applications.," In: EWEA Annual Event 2011. European Wind Energy Association (EWEA); (2011):1-11.

16. U. Fasel, D. Keidel, G. Molinari, P. Ermanni, "Aerostructural Optimization of a Morphing Wing for Airborne Wind Energy Applications," *Smart Materials and Structures*. 26 (2017):1-11.

17. R. Leuthold, "Multiple-Wake Vortex Lattice Method for Membrane-Wing Kites, type=MSc Thesis, organization=Delft University of Technology," (2015). http://resolver.tudelft.nl/uuid:4c2f34c2-d465-491a-aa64-d991978fedf4.

18. P. Thedens, R. Schmehl, "An Aero-Structural Model for Ram-Air Kite Simulations," *Energies*. 16, no. 6 (2023):2603.

19. D. Eijkelhof, G. Buendía, R. Schmehl, "Low- and High-Fidelity Aerodynamic Simulations of Box Wing Kites for Airborne Wind Energy Applications," *Energies*. 16, no. 7 (2023):3008.

20. I. Castro-Fernández, R. Borobia-Moreno, R. Cavallaro, G. Sánchez-Arriaga, "Three-Dimensional Unsteady Aerodynamic Analysis of a Rigid-Framed Delta Kite Applied to Airborne Wind Energy," *Energies*. 14, no. 23 (2021):8080.

21. N. Fonzi, S. L. Brunton, U. Fasel, "Data-Driven Nonlinear Aeroelastic Models of Morphing Wings for Control," *Proceedings of the Royal Society A*. 476 (2020):20200079.

22. M. Folkersma, R. Schmehl, A. Viré, "Boundary Layer Transition Modeling on Leading Edge Inflatable Kite Airfoils," *Wind Energy*. 22, no. 7 (2019):908-921.

23. J. Breukels, R. Schmehl, W. Ockels, "Aeroelastic Simulation of Flexible Membrane Wings based on Multibody System Dynamics," *Airborne Wind Energy. Ser. Green Energy Technol*. Berlin Heidelberg: Springer; (2013):287-305.

24. A. Bosch, R. Schmehl, P. Tiso, D. Rixen, "Dynamic Nonlinear Aeroelastic model of a Kite for Power Generation," *Journal of Guidance, Control, and Dynamics*. 37, no. 5 (2014):1426-1436.

25. M. Buffoni, B. Galletti, J. Ferreau, L. Fagiano, M. Mercangoez, "Active Pitch Control of Tethered Wings for Airborne Wind Energy.," In: 53rd IEEE Conf. Decis. Control. IEEE; (2014):4893-4898.

26. A. Viré, P. Demkowicz, M. Folkersma, A. Roullier, R. Schmeh, "Reynolds-Averaged Navier-Stokes Simulations of the Flow Past a Leading Edge Inflatable Wing for Airborne Wind Energy Applications," *Journal of Physics: Conference Series*. 1618 (2020):1-12.

27. A. Viré, G. Lebesque, M. Folkersma, R. Schmehl, "Effect of Chordwise Struts and Misaligned Flow on the Aerodynamic Performance of a Leading-Edge Inflatable Wing," *Energies*. 15 (2022):1450.

28. M. Folkersma, R. Schmehl, A. Vire, "Steady-State Aeroelasticity of a Ram-Air Wing for Airborne Wind Energy Applications," *Journal of Physics: Conference Series*. 1618, no. 3 (2020):32018.

29. G. D. Fezza, S. Barber, "Parameter Analysis of a Multi-Element Airfoil for Application to Airborne Wind Energy," *Wind Energy Science*. 7 (2022):1627-1640.

30. A. P. Ko, S. Smidt, R. Schmehl, M. Mandru, "Optimization of a Multi-Element Airfoil for a Fixed-Wing Airborne Wind Energy System," *Energies*. 16, no. 8 (2023):3521.

31. K. Vimalakanthan, M. Caboni, J. G. Schepers, E. Pechenik, P. Williams, "Aerodynamic Analysis of Ampyx's Airborne Wind Energy System," *Journal of Physics: Conference Series*. 1037 (2018):62008.

32. J. Mehr, E. J. Alvarez, A. Ning, "Unsteady aerodynamic analysis of wind harvesting aircraft.," In: AIAA Aviation 2020 Forum; (2020):1-13.

33. R. Borobia, G. Sánchez-Arriaga, A. Serino, R. Schmehl, "Flight-Path Reconstruction and Flight Test of Four-Line Power Kites," *Journal of Guidance, Control, and Dynamics*. 41, no. 12 (2018):2604-2614.

34. J. Oehler, R. Schmehl, "Aerodynamic Characterization of a Soft Kite by In Situ Flow Measurement," *Wind Energy Science*. 4, no. 1 (2019):1-21.

35. E. Schmidt, M. De Lellis Costa De Oliveira, R. Saraiva Da Silva, L. Fagiano, A. Trofino Neto, "In-Flight Estimation of the Aerodynamics of Tethered Wings for Airborne Wind Energy," *IEEE Transactions on Control Systems Technology*. 28, no. 4 (2020):1309-1322.

36. R. Borobia-Moreno, D. Ramiro-Rebollo, R. Schmehl, G. Sánchez-Arriaga, "Identification of Kite Aerodynamic Characteristics Using the Estimation Before Modeling Technique," *Wind Energy*. 24, no. 6 (2021):596-608.

37. C. T. Tran, D. Petot, "Semi-empirical model for the dynamic stall of airfoils in view of the application to the calculation of responses of a helicopter blade in forward flight," In: Sixth Eur. Rotorcr. Powered Lift Aircr. Forum; (1980):1-23.

38. J. Leishman, T. S. Beddoes, "A Semi-Empirical Model for Dynamic Stall," *Journal of the American Helicopter Society*. 34, no. 3 (1989):3-17.

39. W. Sheng, W. Chan, R. Galbraith, "Advancement of Aerofoil Section Dynamic Stall Synthesis Methods for Rotor Design," *The Aeronautical Journal*. 116 (2012):521-539.

40. G. Bangga, T. Lutz, M. Arnold, "An Improved Second-Order Dynamic Stall Model for Wind Turbine Airfoils," *Wind Energy Science*. 5 (2020):1037-1058.

41. M. H. Hansen, M. Gaunaa, H. Aagaard Madsen, "A Beddoes-Leishman type dynamic stall model in state-space and indicial formulations," Forskningscenter Risoe, Risoe-R No. 1354(EN); (2004). https://backend.orbit.dtu.dk/ws/portalfiles/portal/7711084/ris_r_1354.pdf.

42. J. Boutet, G. Dimitriadis, X. Amandolese, "A Modified Leishman–Beddoes Model for Airfoil Sections Undergoing Dynamic Stall at Low Reynolds Numbers," *Journal of Fluids and Structures*. 93 (2020):102852.

43. I. Castro-Fernández, F. DeLosRíos-Navarrete, R. Borobia-Moreno, et al., "Automatic Testbed With a Visual Motion Tracking System for Airborne Wind Energy Applications," *Wind Energy*. 26, no. 4 (2023):388-401.

44. F. Palacios, M. R. Colonno, A. C. Aranake, et al. "Stanford University Unstructured (SU2): An open-source integrated computational environment for multi-physics simulation and design," In: 51st AIAA Aerosp. Sci. Meet. Incl. New Horizons Forum Aerosp. Expo.; (2013):1-60.

45. F. Palacios, T. D. Economon, A. C. Aranake, et al. "Stanford University Unstructured (SU 2): Open-source Analysis and Design Technology for Turbulent Flows," In: 52nd Aerosp. Sci. Meet.; (2014):1-33.

46. T. D. Economon, F. Palacios, S. R. Copeland, T. W. Lukaczyk, J. J. Alonso, "SU2: An Open-Source Suite for Multiphysics Simulation and Design," *AIAA Journal*. 54, no. 3 (2016):828-846.

47. K. W. McAlister, S. L. Pucci, W. J. McCroskey, L. W. Carr, "An Experimental Study of Dynamic Stall on Advanced Airfoil Sections Volume 2. Pressure and Force Data," NASA, NASA Technical Memorandum 84245; (1982).

48. J. A. Ekaterinaris, M. F. Platzer, "Computational Prediction of Airfoil Dynamic Stall," *Progress in Aerospace Sciences*. 33, no. 11-12 (1997):759-846.

49. A. Spentzos, G. N. Barakos, K. J. Badcock, et al., "Computational Fluid Dynamics Study of Three-Dimensional Dynamic Stall of Various Planform Shapes," *Journal of Aircraft*. 44, no. 4 (2007):1118-1128.

50. Universidad Carlos III de Madrid, "UC3M-CT Ingenieros flight campaign (April 23)," https://www.youtube.com/watch?v=W9tkuaRj83w; (2023).

51. M. Nardini, "A Computational Multi-purpose Unsteady Aerodynamic Solver for the Analysis of Innovative Wing Configurations, Helicopter Blades and Wind Turbines," (2014). https://core.ac.uk/download/pdf/20526769.pdf.

52. R. Cavallaro, M. Nardini, L. Demasi, "Amphibious prandtlplane: Preliminary design aspects including propellers integration and ground effect," In: 56th AIAA/ASCE/AHS/ASC Struct. Struct. Dyn. Mater. Conf.; (2015):1-27.

53. C. Hirsch, *Numerical Computation of Internal and External Flows*. New York: Wiley; (1984).

54. F. M. White, *Viscous Fluid Flow*. New York: McGraw-Hill; (1974).

55. F. R. Menter, "Two-Equation Eddy-Viscosity Turbulence Models for Engineering Applications," *AIAA Journal*. 32, no. 8 (1994):1598-1605.

56. D. C. Wilcox, *Turbulence Modelling for CFD*. 3rd ed.: DCW Industries; (2006).

57. N. Fonzi, V. Cavalieri, A. D. Gaspari, S. Ricci, "Extended Computational Capabilities for High-Fidelity Fluid–Structure Simulations," *Journal of Computational Science*. 62 (2022):101698.

58. J. D. Eldredge, A. R. Jones, "Leading-Edge Vortices: Mechanics and Modeling," *Annual Review of Fluid Mechanics*. 51 (2019):75-104.

59. C. Martínez-Muriel, G. Arranz, M. García-Villalba, O. Flores, "Fluid-Structure Resonance in Spanwise-Flexible Flapping Wings," *Journal of Fluid Mechanics*. 964 (2023):1-24.

60. K. W. Mangler, J. H.B. Smith, "Behaviour of the Vortex Sheet at the Trailing Edge of a Lifting Wing," *The Aeronautical Journal*. 74 (1970):906-908.

61. B. Thwaites, *Incompressible Aerodynamics: An Account of the Theory and Observation of the Steady Flow of Incompressible Fluid Past Aerofoils, Wings and Other Nodies*. New York: Dover Publications; (1960).

62. W. Sheng, R. A.M. Galbraith, F. N. Coton, "A Modified Dynamic Stall Model for Low Mach Numbers 1," *Journal of Solar Energy Engineering*. 130 (2008):1-10.

Appendix A

Corrected Wake Shedding Direction in UnPam

UnPaM sheds a row of wake panels from the trailing edge in a user-defined direction at every time step of an unsteady simulation [20,52]. Among the infinite existing shedding directions, Mangler and Smith [60] demonstrated that the direction defined by the bisector of the two surfaces gathering at the trailing edge was physically representative for thick bodies. In addition, CFD data visualizations of the RFD kite shows that the flow leaves the trailing edge tangentially to the trailing edge surfaces. An implementation for thin surfaces following Mangler and Smith [60] and the observations in the CFD data has been carried out in this work by defining a preliminary wake shedding direction V'_s as

$$V'_s = \left(\frac{V_A}{V_A} \cdot V_t\right)V_t + \left(\frac{V_A}{V_A} \cdot V_n\right)V_n,$$
$$V_t = \frac{P^{TE}_{i,j+1} - P^{TE}_{i,j}}{\left|P^{TE}_{i,j+1} - P^{TE}_{i,j}\right|}, \quad V_n = \frac{P^{TE}_{i,j} - P^{TE}_{i-1,j}}{\left|P^{TE}_{i,j} - P^{TE}_{i-1,j}\right|}, \quad \text{(A1)}$$

where V_t and V_n are two coplanar unitary vectors defined from three corner points of the trailing edge quadrilateral panels as shown in Figure A1. Equation (A1) represents a projection of the aerodynamic velocity on a plane tangential to the trailing edge surface. Then, a final shedding direction is defined by using part
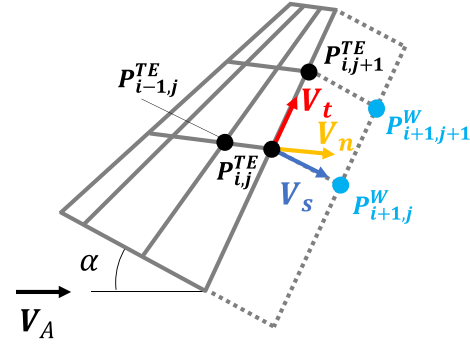

FIGURE A1 | Sketch of a generic wing and shed wake discretized with the vortex lattice method implemented in UnPaM.

of the information from V'_s and canceling the y_W-axis component to avoid nonphysical crossings of wake panels shed by different trailing edge segments,

$$V_s = \frac{V'_s \cdot i_W + V'_s \cdot k_W}{|V'_s \cdot i_W + V'_s \cdot k_W|}. \quad \text{(A2)}$$

This methodology ensures that the shedding direction of every trailing edge panel follows the aerodynamic velocity and is quasi-contained in the panel plane. The first row of wake panels is shed by creating a row of new wake points as

$$P^W_{i+1,j} = P^{TE}_{i,j} + V_A \Delta t V_s, \quad P^W_{i+1,j+1} = P^{TE}_{i,j+1} + V_A \Delta t V_s, \quad \text{(A3)}$$

with Δt the time step of the aerodynamic simulation. The rest of the wake points are displaced by multiplying the total velocity induced by both the kinematic conditions and the singularities placed on the body and wake by Δt. In steady computations, only one row of long wake panels is shed by using Equation (A3) and $\Delta t = \Delta X^W / V_A$, where $\Delta X^W = 50$ m is a user-defined wake length.

Appendix B

State-Space Equations of the Semiempirical Dynamic Stall Aerodynamic Model

Considering the state-space model presented in Section 3.3, the first state equation is a lag equation for the effective angle of attack $\overline{\alpha}$,

$$\overline{\alpha}' = \frac{\overline{\alpha} - \overline{\alpha}'}{T_f}, \quad \text{(B1)}$$

with T_f one of the constant dynamic parameters θ^D that account for the stall delay induced by the pitching motion. The resulting $\overline{\alpha}$ at every time step is used to monitor the leading-edge separation through the detachment of the leading-edge vortex which is triggered at time t_{v0} when conditions $\overline{\alpha} \geq \alpha_{DS}(\dot{\alpha})$ and $\overleftrightarrow{\alpha\alpha} \geq 0$ are met, with

$$\alpha_{DS}(\dot{\alpha}) = \frac{-b_{DS} + \sqrt{b_{DS}^2 - 4a_{DS}\left(c_{DS} - \frac{\dot{\alpha}c_s}{2\overline{V}_A}\right)}}{2a_{DS}}, \quad \text{(B2)}$$

expressed in degrees and a_{DS}, b_{DS}, c_{DS} being fitting parameters from experiments of pitching airfoils directly taken from Boutet et al. [42] (see Table 3).

Another lag equation is needed for the trailing-edge separation point with the same time delay T_f [42],

$$\dot{f}' = \frac{f(\overline{\alpha}) - f'}{T_f}, \tag{B3}$$

where $f(\overline{\alpha})$ was precomputed by using the Kirchhoff model [61]. The latter was used to relate the location of the flow separation point f with the CFD ($C_L^{CFD,S}(\alpha)$) and potential-flow ($C_L^{P,S}(\alpha)$) lift coefficients of the RFD kite for α in static conditions,

$$f(\alpha) = \left(2\sqrt{\frac{C_L^{CFD,S}(\alpha)}{C_L^{P,S}(\alpha)}} - 1\right)^2, \tag{B4}$$

where both coefficients were obtained from precomputed steady lift coefficient versus angle of attack curves with SU2 and UnPaM, respectively. The original Leishman–Beddoes model [38] employed a piecewise fit with three free parameters to approximate the experimental $f(\alpha)$. In this work, due to the abundant CFD and potential-flow data, a linear interpolation was used to look up the lift coefficients in Equation (B4).

The third differential equation governs the lag of the lift coefficient due to the change of circulation for oscillatory motion C_L^v,

$$\dot{C}_L^v = \dot{C}_v - \frac{C_L^v}{T_v}, \tag{B5}$$

with T_v a constant time delay (dynamic parameter θ^D), C_v an estimate of the change in circulation computed as

$$C_v = C_L^{P,Dc} - C_L^f, \tag{B6}$$

where $C_L^{P,Dc}$ is the circulatory part of the potential-flow lift coefficient under dynamic conditions and C_L^f is the unsteady lift coefficient due to the trailing-edge separation process given by

$$C_L^f = C_L^{P,S}(\overline{\alpha})f' + C_L^{fs}(\overline{\alpha})(1 - f'), \quad C_L^{fs}(\overline{\alpha}) = \frac{C_L^{CFD,S}(\overline{\alpha}) - C_L^{P,S}(\overline{\alpha})f(\overline{\alpha})}{1 - f(\overline{\alpha})}, \tag{B7}$$

with C_L^{fs} the fully separated lift coefficient. Equation (B7) computes C_L^f as a weighted average between the fully attached and fully separated lift coefficients [41]. Additionally, this work uses a model originally proposed by Sheng et al. [62] for the overshoot in the lift and pitch moment coefficients due to the leading-edge vortex shedding process,

$$\Delta C_L^v = B_1(f' - f(\overline{\alpha}))V_\chi, \quad \Delta C_m^v = B_2 \Delta C_L^v, \quad V_\chi = \left|\sin\left(\frac{\pi(t - t_{v0})}{2T_{vl}}\right)\right|, \tag{B8}$$

where B_1 and B_2 are two parameters experimentally identified in Boutet et al. [42] (see Table 3). This overshoot is only present from the moment in which the leading-edge vortex detaches from the leading edge (t_{v0}) until the leading-edge vortex clears the trailing edge ($t_{v0} + T_{vl}$, where T_{vl} is another dynamic parameter within θ^D). Additional lift ($C_L^{P,Di}$), drag ($C_D^{P,Di}$) and pitch moment ($C_m^{P,Di}$) coefficients contributions were added in the current work to account for impulsive terms. By summing all the lift contributions, the dynamic stall lift coefficient C_L^{DS} reads,

$$C_L^{DS} = C_L^f + C_L^v + C_L^{P,Di} + \Delta C_L^v. \tag{B9}$$

The dynamic stall drag coefficient was computed by adding unsteady variations to the steady drag computed with CFD $C_D^{CFD,S}$ which already contains 3D and viscous drag effects [41],

$$C_D^{DS} = C_D^{CFD,S}(\alpha) + \Delta C_D^{ind} + \Delta C_D^f + C_D^{P,Di}, \tag{B10}$$

where ΔC_D^{ind} and ΔC_D^f are given by

$$\Delta C_D^{ind} = C_L^{DS}(\alpha - \overline{\alpha}), \quad \Delta C_D^f = (C_D^{CFD,S}(\alpha) - C_{D0}^{CFD,S}) \left[\left(\frac{1 - \sqrt{f'}}{2}\right)^2 - \left(\frac{1 - \sqrt{f(\overline{\alpha})}}{2}\right)^2\right] \tag{B11}$$

and account for the drag induced by the unsteady pitching motion and the pressure drag contribution due to trailing-edge separation, respectively. The latter is computed by multiplying the steady pressure drag, that is, total CFD drag minus a constant viscous drag (zero-lift CFD drag, $C_{D0}^{CFD,S}$, in Table 3), by a modulation factor that depends on the lag between f' and $f(\overline{\alpha})$ [41].

The dynamic stall pitch moment coefficient reads,

$$C_m^{DS} = C_{m0}^{CFD,S} + C_m^f + C_m^v + C_m^{P,Di} + \Delta C_m^v, \tag{B12}$$

where $C_{m0}^{CFD,S}$ is the zero-lift pitch moment obtained from the static CFD data (Table 3), C_m^f and C_m^v are the contributions due to separation and change of circulation, respectively, computed by assuming that C_L^f and C_L^v are applied at the center of pressure of our typical section,

$$C_m^f = C_L^f\left(a - [g(\overline{\alpha}') + 1/4]\right), \quad C_m^v = C_L^v\left(a - [g(\overline{\alpha}') + 1/4]\right), \tag{B13}$$

with $g(\overline{\alpha})$ the position of the center of pressure measured from the quarter-chord of the typical section (see a depiction in Figure 6b) computed as described in Section B.1. To complete the space vector y, the lateral-directional aerodynamic coefficients $C_Y^{DS}, C_l^{DS}, C_n^{DS}$ are given by their potential-flow unsteady counterparts, that is, $C_j^{DS} = C_j^{P,Dc} + C_j^{P,Di}, j = Y, l, n$, as it is assumed that the dynamic stall phenomenon does not affect them.

B.1 | Location of the Center of Pressure

The center of pressure is assumed to be located at the quarter-chord at the zero-lift angle of attack and move downstream as the angle of attack increases (see Figure 6b). In static conditions, this assumption leads to

$$C_m^{CFD,S}(\alpha)\Big|_{1/4c_s} = C_{m0}^{CFD,S}\Big|_{1/4c_s} - C_L^{CFD,S}(\alpha)g(\alpha)\left[\frac{c_s}{c}\right], \tag{B14}$$

with $C_{m0}^{CFD,S}\Big|_{1/4c_s}$ and $C_m^{CFD,S}(\alpha)\Big|_{1/4c_s}$ the zero-lift and current (at α) pitch moment coefficients about the quarter-chord computed with SU2. From Equation (B14), $g(\alpha)$ is isolated,

$$g(\alpha) = \frac{C_{m0}^{CFD,S}\Big|_{1/4c_s} - C_m^{CFD,S}(\alpha)\Big|_{1/4c_s}}{C_L^{CFD,S}(\alpha)\left[\frac{c_s}{c}\right]}. \tag{B15}$$

Leishman and Beddoes [38] approximated g with a four-parameter fit of experimental data. In the current work, the values for $C_{m0}^{CFD,S}\big|_{1/4c_s}$, $C_m^{CFD,S}(\alpha)\big|_{1/4c_s}$ and $C_L^{CFD,S}(\alpha)$ were looked up from a steady RANS database precomputed with SU2.

Appendix C

Analysis of the Relative Error Among the Three Aerodynamic Tools

An error analysis of the three aerodynamic tools under unsteady conditions is addressed in this section. The pitching motion ($\dot{\alpha} \neq 0$) of Section 4.2.1 is considered and the results from the three tools shown in Figure 10 are compared. Figure C1 displays the evolution of the relative errors in the lift (a) and drag (b) coefficients together with the prescribed angle of attack during one dynamic stall cycle. As pointed out in Section 4.2.1, the potential-flow method presents high errors ($\sim 40\%$ in C_L and $\sim 35\%$ in C_D) as compared with unsteady RANS having the maxima during the downstroke because the potential-flow hysteresis cycle is in the opposite direction. The relative error of the semiempirical dynamic stall tool is within 7% and 3% for C_L and C_D, which remarks the good match between this method and unsteady RANS.
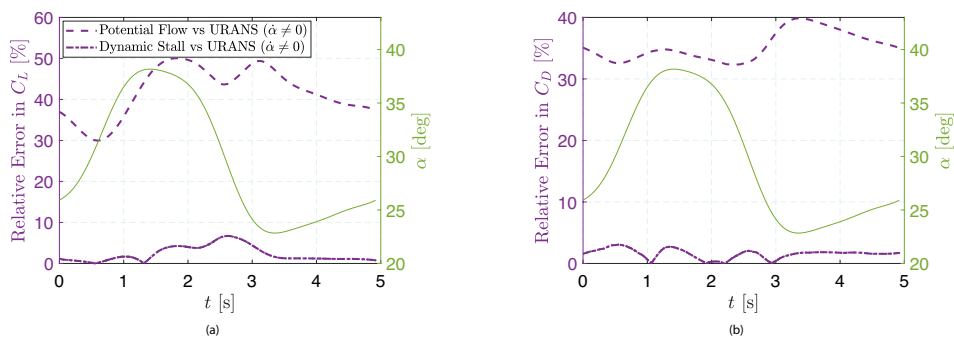

FIGURE C1 | Evolution of α (right axes) and the relative error (left axes) in the lift (a) and drag (b) coefficients computed with the potential-flow and dynamic stall methods with respect to URANS during dynamic stall cycle 2 in Figure 4